Deformation modes in an Icelandic basalt: From brittle failure to localized deformation bands

M. Adelinet [*,1], J. Fortin, A. Schubnel, Y. Guéguen

Laboratoire de géologie, École normale supérieure, 24 rue Lhomond, 75005 PARIS, UMR CNRS 8538, France

ARTICLE INFO

ABSTRACT

According to the stress state, deformation mode observed in rocks may be very different. Even in the brittle part of the crust a differential stress can induce shear failure but also localized compacting deformation, such as compaction bands in porous sedimentary rocks. The mode of deformation controls many hydrodynamic factors, such as permeability and porosity. We investigate in this paper two different modes of deformation in an Icelandic basalt by using laboratory seismological tools (elastic waves and acoustic emissions) and microstructural observations. First of all, we show that at low effective confining pressure ($P_{eff} = 5$ MPa) an axial loading induces a shear failure in the basalt with an angle of about 30° with respect to the main stress direction. On the contrary, at high effective confining pressure ($P_{eff} \geq 75$ MPa and more) an increase of the axial stress induces a localization of the deformation in the form of subhorizontal bands again with respect to the main stress direction. In this second regime, focal mechanisms of the acoustic emissions reveal an important number of compression events suggesting pore collapse mechanisms. Microstructural observations confirm this assumption. Similar compaction structures are usually obtained for porous sedimentary rocks (20–25%). However, the investigated basalt has an initial total porosity of only about 10% so that compaction structures were not expected. The pore size and the ratio of pore to grain size are likely to be key factors for the particular observed mechanical behavior.

© 2013 Elsevier B.V. All rights reserved.

1. Introduction

Basaltic rocks are the main component of the oceanic upper crust. During cooling, the basalt lava flow is highly fractured. Thus, at shallow depth they can host fluids (Geoffroy and Dorbath, 2008; Adelinet et al., 2011a, 2011b). This is of potential interest in water resources (D'Ozouville et al., 2008) or in CO_2 storage issues (Matter et al., 2007; Goldberg et al., 2008). Elastic properties of basalt have been investigated in the laboratory through different experiments: (i) evolution of elastic parameters during increasing confining pressure (Vinciguerra et al., 2005; Stanchits et al., 2006; Adelinet et al., 2010; Fortin et al., 2011) and (ii) differential stress cycling (Vinciguerra et al., 2005; Heap et al., 2009) and also (iii) evolution related to increasing temperature (Pinkerton and Norton, 1995; Lore et al., 2000; Kato et al., 2003; Violay et al., 2010, 2012). In addition, in order to constrain the behavior of natural volcanic systems (during pre- and post-eruptive time intervals notably), some experimental studies of rupture have also been performed on volcanic rocks (Rocchi et al., 2002, 2004; Balme et al., 2004; Smith et al., 2009).

Beyond a defined stress threshold, rock deformation becomes irreversible. Then the increasing differential stress can induce a non-elastic deformation of the rock. Different deformation regimes are possible. Dilatancy and brittle faulting typically result in shear bands characterized by stress softening (Paterson, 1978). A fundamentally different failure mode develops if a porous rock is stressed under relatively high confinement and low temperature. The pore space compacts and ductile failure develops. In this ductile regime, characterized by strain hardening, damage can be distributed in non-localized manner (Handin and Hager, 1963; Wong et al., 1997) or can be localized, i.e. under the form of compaction bands. Compaction bands are areas of material which extend perpendicular to the main compressive stress. From microstructural observations, a compaction band appears as a crushed zone of reduced porosity. Such structures have only been observed up to now in the laboratory in porous sedimentary rocks (Klein et al., 2001; Wong et al., 2001; Baud et al., 2004; Fortin et al., 2006, 2009) or in porous material like honeycombs (Papka and Kyriakides, 1998) or aluminum foams.

These different regimes correspond to specific stress conditions characterizing the yield envelope of the rocks in the (P,Q) plane, where P is the mean effective pressure and Q the differential stress. Laboratory conditions allow sometimes to describe the full yield envelope of a rock, as for some limestones or sandstones (Wong et al., 1997; Baud et al., 2004; Vajdova et al., 2004; Fortin et al., 2005, 2006, 2009). At low confining pressure, these rocks exhibit a brittle behavior. At higher confining pressure, increasing axial stress induces the formation of compaction bands. However, at room temperature

---

* Corresponding author at: IFP Énergies Nouvelles, 1-4 avenue Bois Préau, 92852 Rueil-Malmaison Cedex, France. Tel.: +33 147527142.

E-mail address: mathilde.adelinet@ifpen.fr (M. Adelinet).

[1] Now at IFP Énergies Nouvelles, 1-4 avenue Bois Préau, 92852 Rueil-Malmaison Cedex, France.

only brittle regime has been observed on basalts (Stanchits et al., 2006; Benson et al., 2007, 2008; Heap et al., 2011). Note that Violay et al. (2012) shows that basalt submitted to high temperature exhibits a ductile behavior even at low confining pressure.

Deformation in rocks is not only controlled by the differential stress Q but also by the effective pressure P and is consequently related to the fluid pressure (Secor, 1965), as the effective pressure is defined by the mean stress minus the pore pressure. Note that pore pressure is one of the most variable parameter in the earth crust. The role of pore fluid in the mechanics of the crust has been extensively studied in the past (Rocchi et al., 2002; Kato et al., 2003; Balme et al., 2004; Ramsey and Chester, 2004). More recently, a specific fluid-induced rupture experiment was performed on a Fontainebleau sandstone recording acoustic emissions (Schubnel et al., 2007).

This paper presents the results of triaxial experiments performed on an Icelandic basalt. Depending on the confining and fluid pore pressure values, different deformation modes have been evidenced. Strain and elastic wave velocities have been measured. Simultaneously, we recorded acoustic emissions to monitor and analyze the failure processes. Microstructure analysis of deformed samples has also been conducted and correlated to acoustic emissions locations.

2. Samples and experimental methods

2.1. The Reykjanes basalt

2.1.1. Description of investigated basalt

The basaltic block was extracted on a road outcrop in the Reykjanes peninsula (southwestern part of Iceland), in the vicinity of the road connecting the cities of Keflavik and Vogar. Due to its particular geological context, Iceland is the ideal natural laboratory to study interplays between fluid, basalt and deformation. Extracted samples were fresh and young (less than 10,000 years; Sigurdsson et al., 2000). The studied rock is a microlitic alkali basalt containing mm-sized phenocrysts of pyroxene and albite (identified with X-ray method, see Fig. 1B) and also microliths of feldspar (thin section in Fig. 1A). We also investigate the microstructure and the chemical composition of an intact Reykjanes sample through a Scanning Electron Microscope (SEM) installed at the Laboratoire de Géologie of École Normale Supérieure (Paris, France). The chemical composition of the microlitic matrix is presented in Table 1 in oxide weight percentage. Fig. 2 present a large scale view of the microstructure (top figure) and a detail of a pore where we the microlitic texture (bottom figure) can be identified. The mean size of

grains is about 100 μm. At the resolution of optical and electron microscopes, neither phenocrysts of pyroxen and albite nor feldspar microliths appear cracked.

2.1.2. Porosity analysis

Based on mercury intrusion porosimetry data, the sample presents a bimodal distribution of porosity. Initial porosity is about 8% made up of 1% crack porosity and 7% equant pores. This bimodal distribution confers some interesting properties to the rock in terms of elastic wave velocity dispersion for instance (Adelinet et al., 2010). Note that more details on mercury porosimetry results are presented in Adelinet et al. (2010). The average inclusion entry diameters are 0.1 and 100 μm, respectively for cracks and pores. The porosity accessible to helium gas of the Reykjanes basalt has been investigated by He-pycnometry (equipment installed at IFP Energies Nouvelles). The porosity value is $10.3 \pm 1\%$. Note that the porosity values of the Reykjanes basalt range is typical for basaltic rocks coming from lava flows (Saar and Manga, 1999). Around 2% of the porosity is unconnected to mercury but connected to helium gas. The difference can be explained by the different sizes of helium and mercury molecules according to surface tension. Very thin cracks accessible to helium are not accessible to mercury. Furthermore volatile exsolution during magma ascent can lead to isolated vesicles which are not accessible to gases or liquids. Additional processes such as thermal cooling can induce thin cracks to the magma eventually connecting some of these isolated vesicles. Consequently, depending on their aperture, cracks are accessible to gas only or gas and liquid leading to a difference in porosity measurements.

2.2. Experimental set-up

Cylindrical specimens of 80 mm in length and 40 mm in diameter were cored into the Reykjanes basalt block. The experiments were performed in a triaxial cell installed at the Laboratoire de Géologie of École Normale Supérieure (Paris, France) and exhaustively described in Ougier-Simonin et al. (2011) and Brantut et al. (2011). A schematic diagram of the setup is presented in Fig. 3. This apparatus allows for hydrostatic and differential stresses to be applied independently on the cylindrical sample. The hydrostatic and differential stresses are servo-controlled with an accuracy of 0.01 MPa. The confining medium is oil. Pore pressure is driven by one precision volumetric pump. Pore fluid is introduced into the sample through hardened steel end pieces placed on the top and bottom of the rock sample. Maximum pore pressure in the system is 100 MPa. Axial strain is measured by three gap sensors
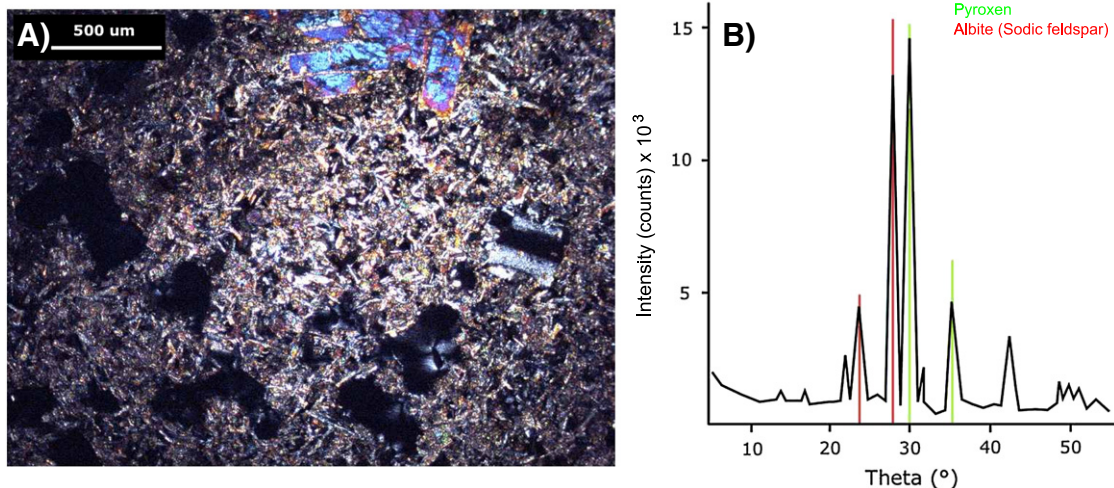

Fig. 1. Petrographical description of the Reykjanes basalt: A) thin section picture showing the microlithic texture with phenocrystals of pyroxen and the equant porosity, B) X-ray diffractogram.

Table 1
Chemical composition of the microlitic matrix observed on an intact sample of the Reykjanes basalt. Data are expressed in oxide weight percentage.

Na_2O	MgO	Al_2O_3	SiO_2	CaO	TiO_2	FeO
1.91	7.52	16.29	51.34	12.44	0.80	9.68

mounted externally and also locally by strain gauges glued directly to the sample. Strain gauges allow also to measure local radial strain. Uncertainty in strain measurements was estimated to be 10^{-5} for external strain data and 10^{-6} for strain gauges data. In addition, if the pore pressure is kept constant, the variation of the pore volume during a test allows the evolution of volumic strain to be monitored.

A network of 16 piezoceramic transducers is used to measure high frequency P-wave velocities along several directions. Using this network, acoustic emissions (AE) were captured by the ASC© GigaRecorder (Mini Richter system), which stores continuous ultrasonic waveform data onto a 1 TB hard disk. AE absolute source locations were obtained with an average accuracy of 2 mm using a homogeneous transversely isotropic velocity profile. Source focal mechanisms are also deduced from moment tensor data (first motion polarization and amplitude of the first P-wave arrivals).

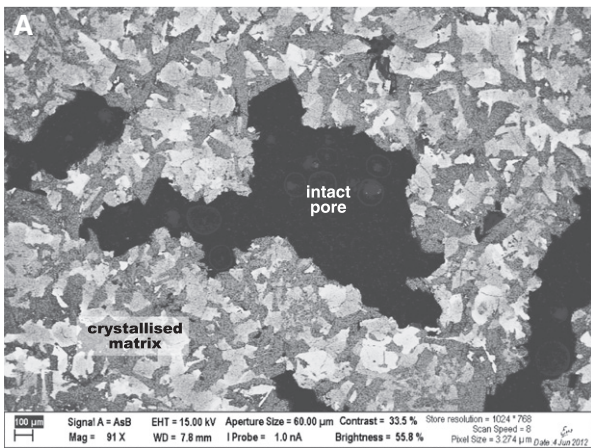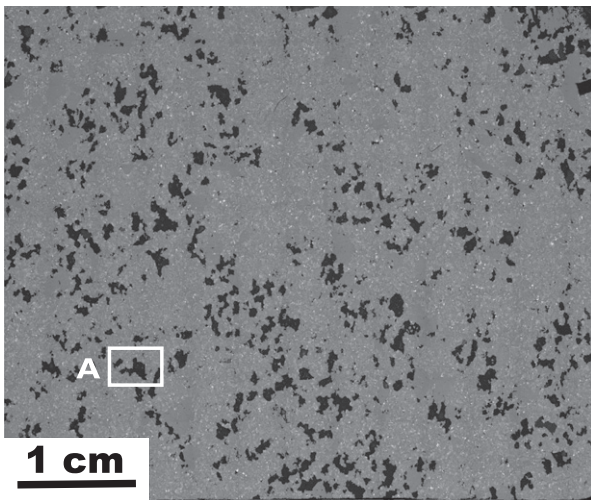**Fig. 3.** Schematic diagram of the triaxial cell ST100.

Fig. 2. SEM pictures of the intact Reykjanes basalt. Detail a has been subjected to an image processing to enhance the contrast between pore space and microlitic matrix. Grain size and pore size are respectively about 100 μm and 1 mm.
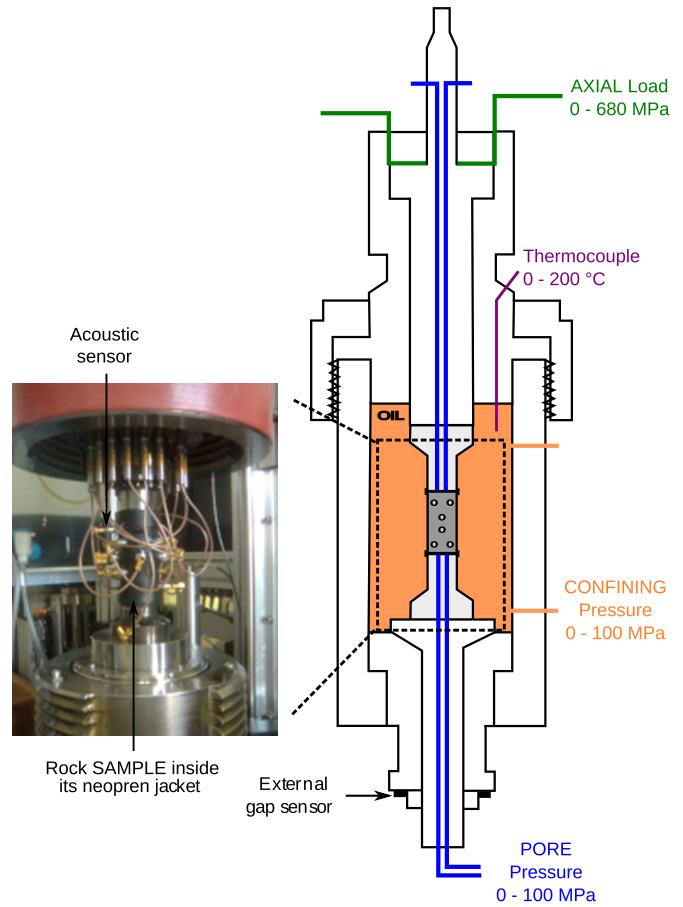
All experiments were carried out at room temperature and at a constant axial strain rate of 10^{-6} s^{-1}. The confining and pore pressures are respectively denoted by P_c and P_p. Hereafter results from four experiments would be presented. The different experimental conditions are summarized in the following list and in Table 2:

- experiment T1: $P_c = 10$ MPa, $P_p = 5$ MPa
- experiment T2: $P_c = 80$ MPa, $P_p = 5$ MPa
- experiment T3: $P_c = 100$ MPa, $P_p = 5$ MPa
- experiment T4: $P_c = 80$ MPa, $Q = 120$ MPa and the pore pressure is increased until reaching failure.

Table 2
Compilation of mechanical data for Reykjanes basalt: confining pressure P_c, pore pressure P_p, effective mean pressure (P) and differential stress (Q) values for the critical stress state C' and the peak stress (T1–T4); and the critical stress state C^* (T2–T3). Samples deformed during T1 and T4 failed by shear localization whereas samples deformed during T2 and T3 failed by localized deformation bands.

Test	P_c (MPa)	P_p (MPa)	Onset of dilatancy C'		Peak stress	
			P (MPa)	Q (MPa)	P (MPa)	Q (MPa)
T1	10	5	20	45	45	120
T4	80	76	18	42	43	118

Test	P_c (MPa)	P_p (MPa)	Onset of compaction C^*	
			P (MPa)	Q (MPa)
T2	80	5	156	243
T3	100	5	186	273

3. Results

3.1. Mechanical and velocities data

We use the convention that compactive strains and compressive stresses are positive. Maximum and minimum principal stresses are respectively denoted by σ_1 and σ_3. The effective mean pressure $\frac{\sigma_1 + 2\sigma_3}{3} - P_p$ is denoted by P and the differential stress $\sigma_1 - \sigma_3$ by Q. We also introduce two specific states, C' and C^* as presented in Wong et al. (1997): beyond the critical stress state C' the differential stress field is responsible for pore space dilation (commonly observed in brittle failure regime) and beyond the critical stress state C^* the differential stress field results in significant contribution to the irreversible compactive strain.

Fig. 4 reports mechanical data obtained during experiments T1, T2 and T3: volumetric strain versus effective mean stress (Fig. 4a) and axial strain versus differential stress (Fig. 4b). The deformation observed for the experiment performed at 10 MPa of confining pressure (T1) is characteristic of the brittle failure regime. The differential stress reaches a peak stress just before the macroscopic failure occurs. We identify the critical state C' from which the compaction begins to reverse into dilation, with respect to the hydrostatic state. For experiments T2 and T3 performed at high confining pressure, a critical stress level C^* is observed, from which the differential stress induces a significant irreversible compactive strain, described in Wong et al. (1997) as shear-enhanced compaction. Experiment T2 has been stopped just after reaching the C^* point at an axial strain of 1.4%. Experiment T3 has been performed up to an axial strain of 2.7%. Beyond C^*, the strain–stress curve exhibits several drops (Fig. 4b).

The following section shows that the acoustic emissions rate can be correlated to these stress drops (Fig. 7). Table 2 summarizes the critical stress state C' and the peak stress for experiments T1 and T4; and the critical stress state C^* for experiments T2 and T3. These values allow us to propose a yield envelope for the Reykjanes basalt, as discussed below in Section 3.2.4.

Fig. 5 reports the axial P-wave velocity data of experiments T1 and T3 as functions of differential stress Q. The figure shows also the volumetric strain versus Q. For test T1 (Fig. 5A), the axial P-wave velocity remains almost constant at 5400 m·s^{-1} until the stress state reaches the critical level C'. Then velocity decreases from 5450 to 5100 m·s^{-1} just before the failure occurs. The evolution of the velocity is in agreement with

the evolution of the volumetric strain: during the axial loading, microcracks nucleate and propagate leading to dilatancy and a decrease of the velocity. Once failure is reached, P-wave velocity sharply decreases to the value of about 4500 m·s^{-1}. Fig. 5B shows the evolution of the P-wave velocity during the experiment T3 performed at $P_c = 100$ MPa. We observed the same behavior for experiment T2. At the beginning of the axial loading, velocity tends to slightly increase to the value of about 5700 m·s^{-1}, probably due to the closure of pre-existing cracks. However, once the stress state is close to the critical stress C^*, velocity decreases, whereas inelastic compaction is observed. This result is in agreement with the observation done on porous sandstone (Fortin et al., 2005) and illustrates the complex correlation between porosity and elastic properties. It can be explained by two simultaneous processes: pore collapse and crushing of the surrounding material.

3.2. Acoustic emissions (AE)

The experimental set-up available at ENS allows to record acoustic emissions (AE) continuously. However, due to the limitation of the hard disk (1 TB), this record is limited to about 1 h. For longer experiments the AE are triggered. Thus for experiments T1 and T2, AE were continuously recorded and acoustograms are available (Section 3.2.1). T3 was a longer experiment (5 h), thus only the AE rate is presented (Section 3.2.2). Note that in the 3 experiments, the AEs can be located (Section 3.2.4).

3.2.1. Acoustograms

Based on mechanical data gained in our experiments two different deformation modes could be identified, a brittle failure one and a ductile one. These two modes are very different on the macroscopic scale, but they both involve microcracks at grain-scale, as seen from the elastic wave velocity behavior. As a consequence these two regimes lead to radiation of acoustic emissions. The AE activity during rock deformation is due to damage processes, such as microcracking or pore collapse. Fig. 6 presents the acoustograms obtained during the experiments T1 ($P_c = 10$ MPa) and T2 ($P_c = 80$ MPa). AE continuous recording involves very large recorded data size, so that it was performed only for the 100 s interval containing the maximum of deformation. This figure shows that there two very different acoustic signatures for the Reykjanes basalt. They depend strongly on the stress field applied to the rock. Indeed, for test T1 the pre- and post-failure activities are very weak. The majority of the AEs are generated only during one burst occurring just before the macroscopic failure.

3.2.2. AEs rate

We investigated the AE rate evolution during the experiment T3 ($P_c = 100$ MPa). The results are plotted in Fig. 7 that shows the AE rate recording during about 5 h and the differential stress versus strain. Fig. 6 focuses on the 100 s just before the maximum strain. Fig. 7 shows the AE activity occurring during the full experiment. The AE rate increases before C^* and drops just after this critical stress state. Beyond C^*, several surges of AE events can be seen and can be correlated to stress drops. Fig. 7 is comparable to the observations done on Bentheim sandstone by Baud et al. (2004) in which compaction bands were observed. In both cases, the overall hardening trend is punctuated by episodic stress drops which are associated with surges in AE rate. Baud et al. (2004) interpreted each individual stress drop event as an unstable propagation of a compaction band normal to the axial stress associated to intensive grain-scale cracking that induces a burst of AEs.

3.2.3. AE focal mechanisms

To characterize the source type from the moment tensor, we need to introduce two parameters, k and T which are expressed as functions of the three real eigenvalues and the trace of the moment tensor (Hudson et al., 1989). Both quantities vary between -1 and 1. The pure double couple sources are described by $k = T = 0$. If $k = 1$, the
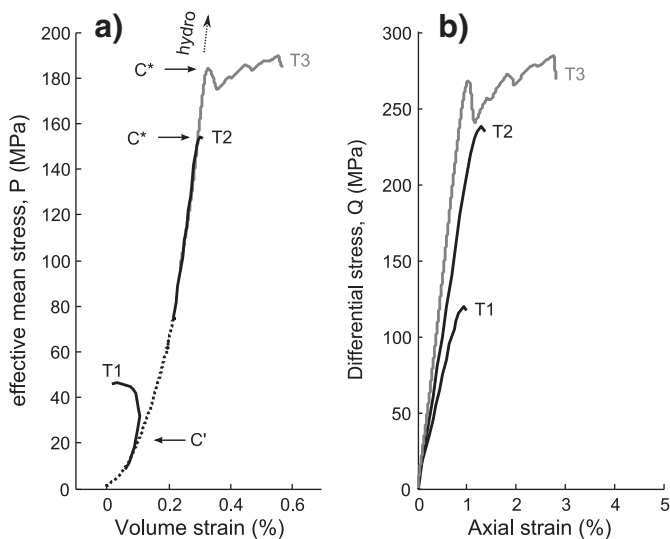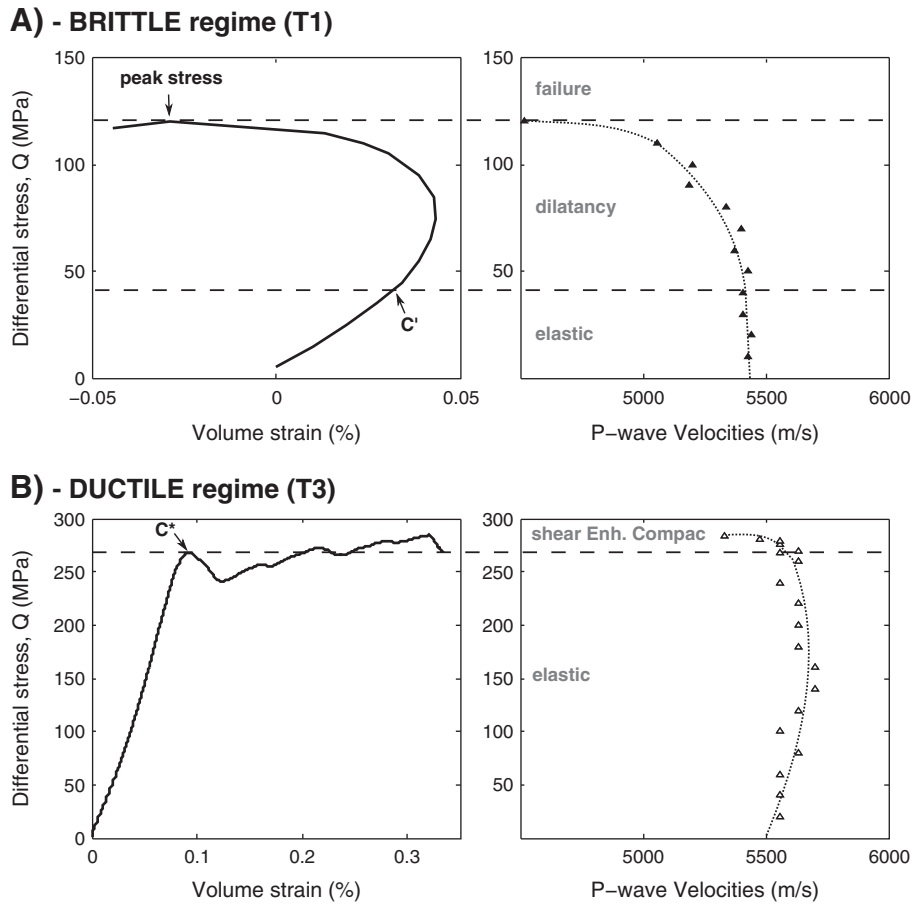

Fig. 4. a — Volumetric strain as a function of effective mean stress for experiments T1, T2 and T3. For reference, the hydrostat is shown in dashed curves. The critical stress states C' and C^* are indicated by the arrows. b — Axial strain as a function of differential stress for experiments T1, T2 and T3.

Fig. 5. Differential stress as functions of volume strain and P-wave velocity for experiment T1 (top) and T3 (bottom). The critical stress states C′ and C* are indicated by the arrows. 'Shear Enh. Compac.' is for Shear Enhanced Compaction, the deformation mode observed after C* for T3 (and also T2).
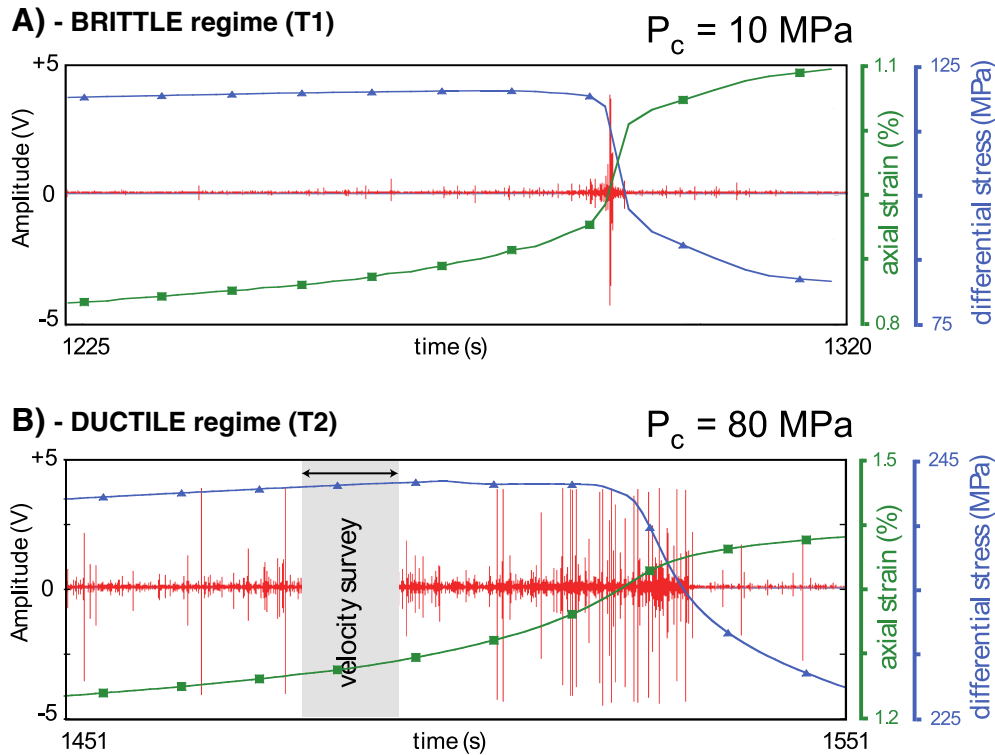

Fig. 6. Acoustograms obtained for experiments T1 and T2 on about 100 s during which respectively peak stress and C* is reached. Strain and stress are also reported, respectively in green and blue.
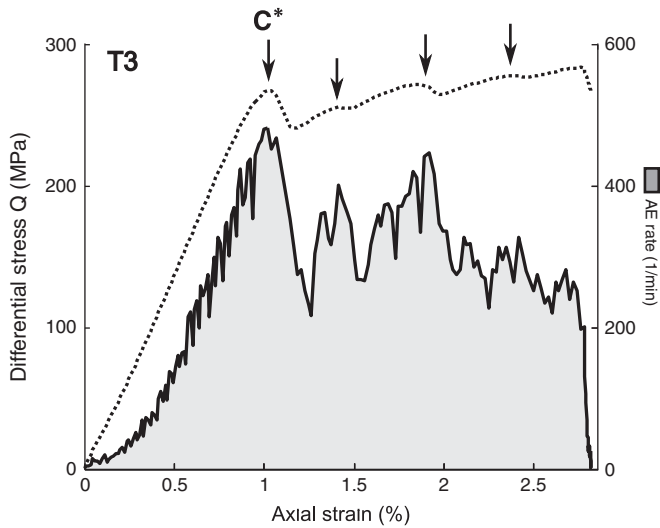
Fig. 7. Acoustic emission rate (solid curve) and differential stress (dotted curve) as functions of axial strain in Reykjanes basalt during test T3. Stress peaks correlated with burst of acoustic emissions are indicated by the arrows.

source is purely explosive while $k = -1$ corresponds to a pure implosion (Baig and Urbancic, 2010).

The variety of source mechanisms obtained during experiments T1 and T2 are illustrated in Fig. 9 in the Hudson diagram, also called source-type diagram. The vertical axis represents k and T is on the parallel axis. This diagram has a peculiar shape in order to ensure the even probability distribution of source types. Double-couple mechanisms are located in the center, purely explosive and implosive events are at the top and the bottom of the parallelogram respectively. Thus, whereas most of events recorded during T1 are shear events, a largest number of the events recorded during T2 are in the compression part of the diagram. The focal mechanisms observed during compaction of the Reykjanes basalt are in agreement with the observation done on the

acoustic signature of porous sandstones (Wong et al., 1997; Baud et al., 2004; Fortin et al., 2009).

3.2.4. AE location

The locations presented in Fig. 8A reveal that AEs are located on an inclined plane with an angle of about 30° with respect to the main stress direction, characteristic of the brittle failure. Conversely, the acoustic background noise is much more pronounced for the experiments at high confining pressure (Fig. 6B). The AEs are not located on a plane but in a cluster located in the central part of the sample (Fig. 8B). For the most precisely located events we investigated the focal mechanism of the source.

Fig. 10 reports results of the location and focal mechanisms obtained for experiment T3. Only the AEs located on a plane crossing transversally the center part of the sample have been represented. Note that the majority of the AEs are located in the white areas corresponding to material crushing areas. Focal mechanisms are represented with the following color code: in orange, events with a main shear component, in blue and green, events with respectively a main compressive and tensile component. In the material crushing areas, both shear and compressive events are present. The next section focuses on the microstructure analysis related to these different mechanisms based on SEM pictures.

3.3. Microstructure

Fig. 11 presents macroscopic views of intact and deformed samples. For intact, T2 and T4 samples, it consists of simple photographs of external sample views. For T3, it is a picture of the sagittal cross section. Finally for T1, the view is an X-ray scan picture emphasizing the shear failure. The brittle behavior is clearly visible for T4 sample. The failure occurs with a classical angle of about 30° with respect to the main stress direction, splitting the sample into two pieces. Shear failure also occurs during test T1. However we stopped axial loading just after the first evidence of rupture so that the fault plane is only visible on the X-ray scan sagittal cross section. Another mode of deformation is clearly observed on T2 and T3 samples. White structures are plainly visible in the central part
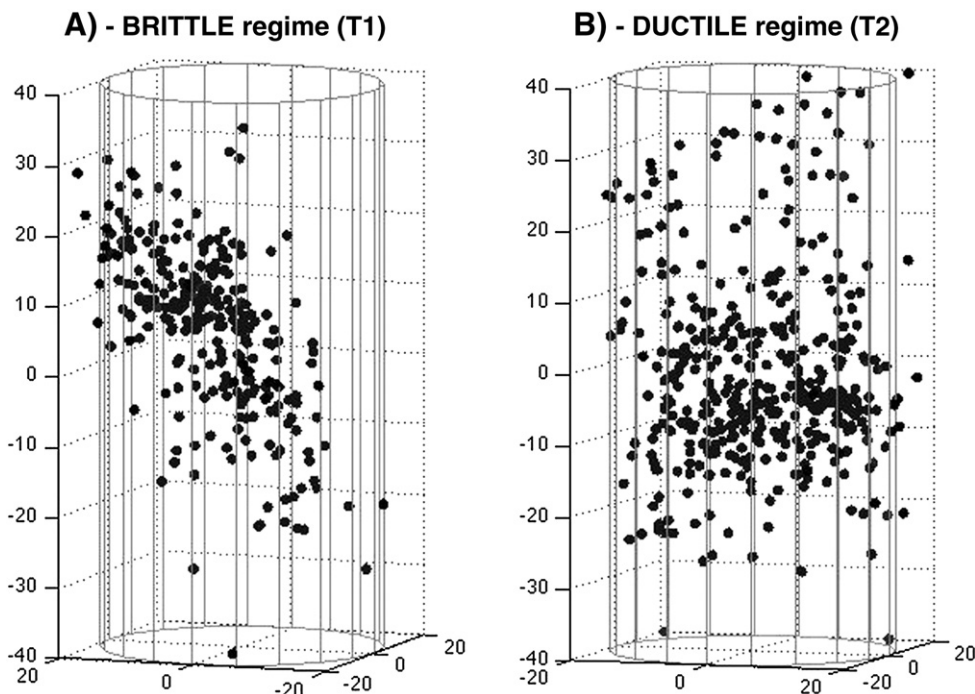

Fig. 8. 3D view of the sample with AEs localizations for test T1 (left) and test T2 (right). Respectively the 271 and 407 biggest events are located into the 3D structure. Note that AEs are located along an oblique shear plane for test T1 and in the central part of the sample for test T2.
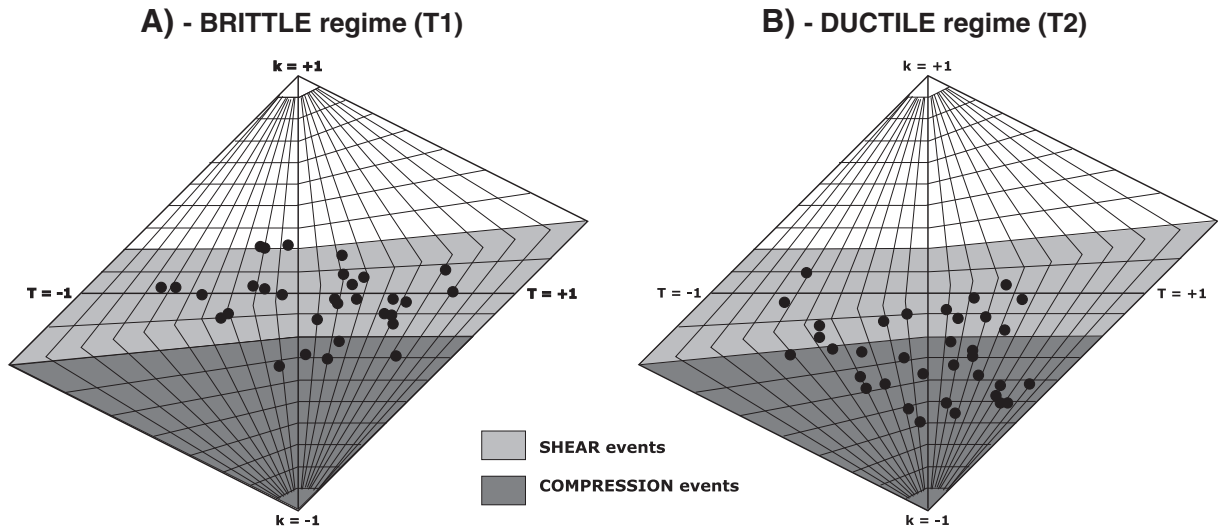
Fig. 9. Focal mechanisms deduced from the biggest acoustic emissions during test T1 (left part) and test T2 (right part). Focal mechanisms are plotted in the Hudson diagram (Hudson et al., 1989). Shear and compression areas are respectively represented in light gray and dark gray.

of the sample. These structures might be interpreted as thick deformation bands (between 2 and 3 mm). The white zones are approximately subhorizontal and present crenulations at a smaller scale. White color is due to crushing of the materials. The macroscopic view of the sample deformed during test T3 (performed at $P_c = 100$ MPa) is very similar to that of the sample deformed during test T2 (performed at $P_c = 80$ MPa).

Figs. 12 and 13 are SEM pictures taken respectively on samples T1 and T2. Fig. 12 illustrates the damage evolution in the sample that failed by shear localization. During compression loading equant pores induce tensile stresses, which initiate vertical cracks (Fig. 12A). With an increase of differential stress, vertical cracks propagate and coalesce leading to the development of shear zones. Two shear zones are observed in Fig. 12, the first seem to be stopped by an equant pore (Fig. 12B) whereas the second one lead to the macroscopic failure of the sample. The central part of the shear zone shows grain crushing (Fig. 12C), in agreement with previous observations (Stanchits et al., 2006; Benson et al.,
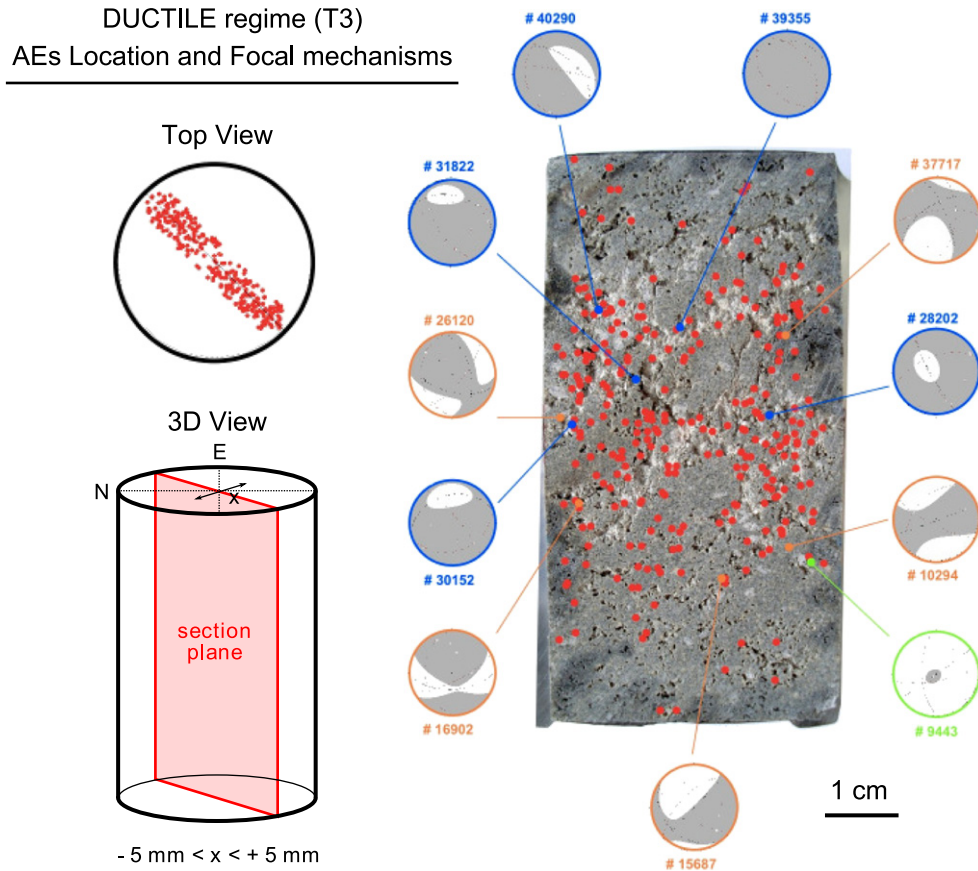

Fig. 10. Focal mechanisms and locations of acoustic emission recorded in the center part of the sample during test T3. Orange, blue and green circles correspond respectively to events with a main shear, compressive and tensile component.
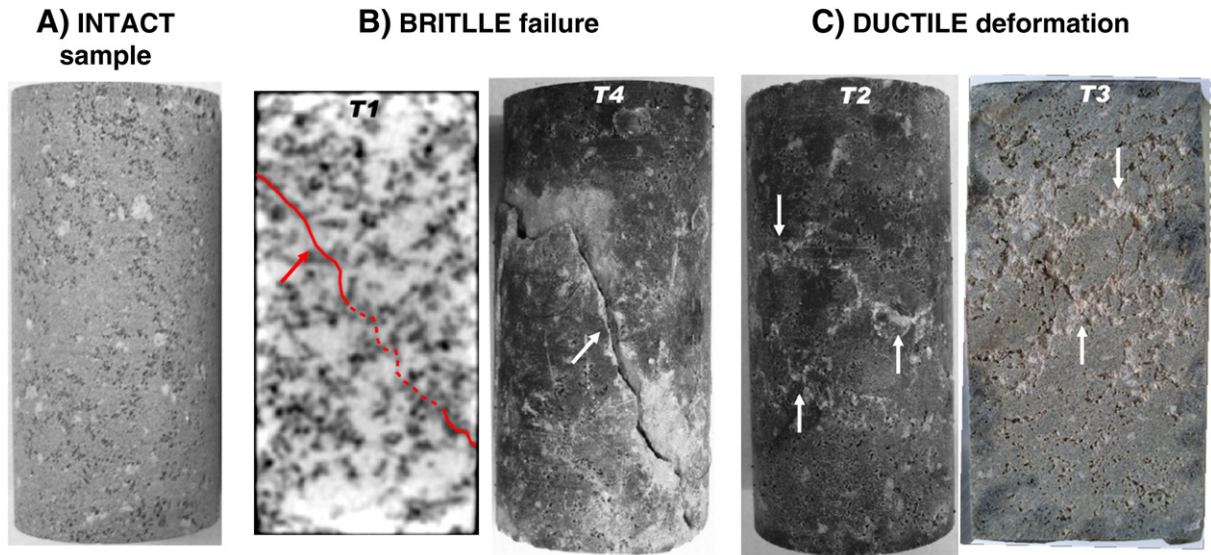
Fig. 11. Macroscopic views of the deformation observed in the Reykjanes basalt. Red and white arrows emphasize modes of deformation to observe on each sample. (A) Intact sample. Initial sample diameter is 40 mm and length is 80 mm. (B) samples showing brittle behavior: X-scan view of T1 sample ($P_c = 10$ MPa and $P_p = 5$ MPa) and macroscopic view of T4 sample ($P_c = 80$ MPa and $P_p = 75$ MPa). As T1 sample does not break at macroscale, the shear plane is only visible on X-scan pictures. Conversely, the macroscopic failure is clearly visible for T4 sample, it is broken into two distinct pieces. (C) samples showing ductile deformation: view of T2 sample ($P_c = 80$ MPa and $P_p = 5$ MPa) and T3 sample ($P_c = 100$ MPa and $P_p = 5$ MPa) on a sagittal cross section, localized compaction areas appear in white due to pore collapse.
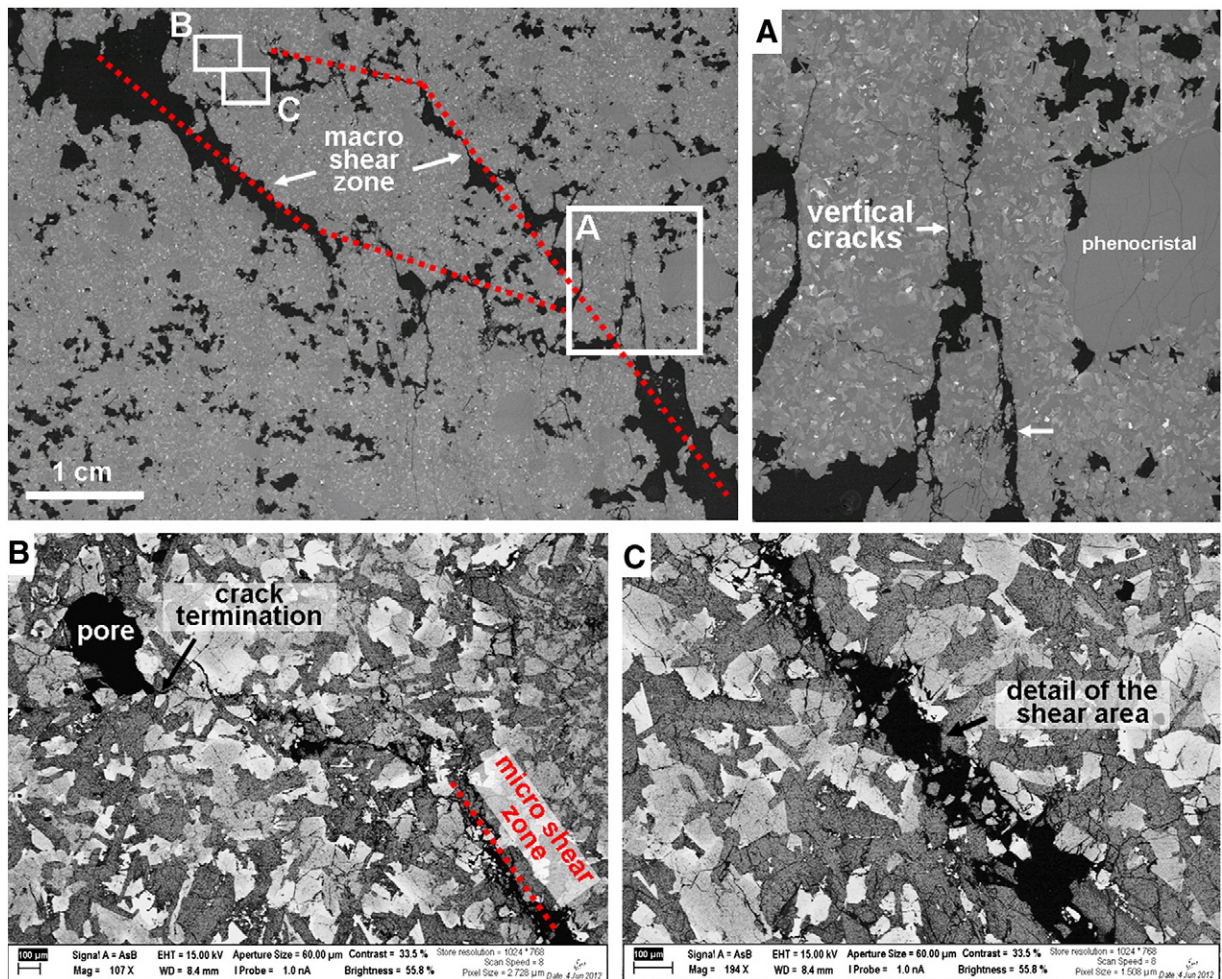

Fig. 12. SEM pictures taken on the sample deformed in test T1. The mean stress inducing rupture is vertical. A: Detail of early vertical crack network. B and C: SEM pictures obtained after image processing to enhance the details of the shear zone. Note the termination of cracks within pores.

2007, 2008; Heap et al., 2011). Fig. 13 presents SEM pictures corresponding to the sample deformed at 75 MPa effective confining pressure. In these pictures, a clear sub-horizontal deformation band is visible and is indicated by white arrows (Fig. 13A). Fig. 13B and c clearly show pore collapses. These pore collapses induce crushing of the surrounding material. For example, in Fig. 13B the limit of the former pore is visible but almost all the volume is filled with small grains.

Fig. 13C is a picture taken with secondary electron and allows to visualize the 3D microstructure. In this case, the pore is not totally filled with fine material but it is elongated perpendicular to the main stress direction. Cracks seem to be nucleated at the edge of the collapsed pores. They propagate sub-perpendicularly to the maximum compressive stress direction (which is vertical on the pictures). As a consequence, localization of the compaction in a porous basalt seems to be the result of pore collapse and propagation of sub-horizontal shear cracks. This mechanism is in agreement with the AEs focal mechanisms (Fig. 9B). Compaction events are mainly the result of pore collapse whereas shear events may be due to propagation of subhorizontal shear cracks between the collapsed pores.

Moreover, some information on the chemistry of the infilled grains are inferred from an ion microprobe associated to SEM. Aluminum and silicium are predominant in the composition. Based on the initial composition, we assume that the major part of the infilled grains come from feldspar microliths. This observation is in agreement with some other studies done on basaltic rocks. Indeed, Cordonnier et al. (2009) show that feldspars crushed under an increasing of stress, in three 3 main stages: initial crystal, puzzle form, powder and flow banding. In our experimental conditions, we probably reached the puzzle stage.
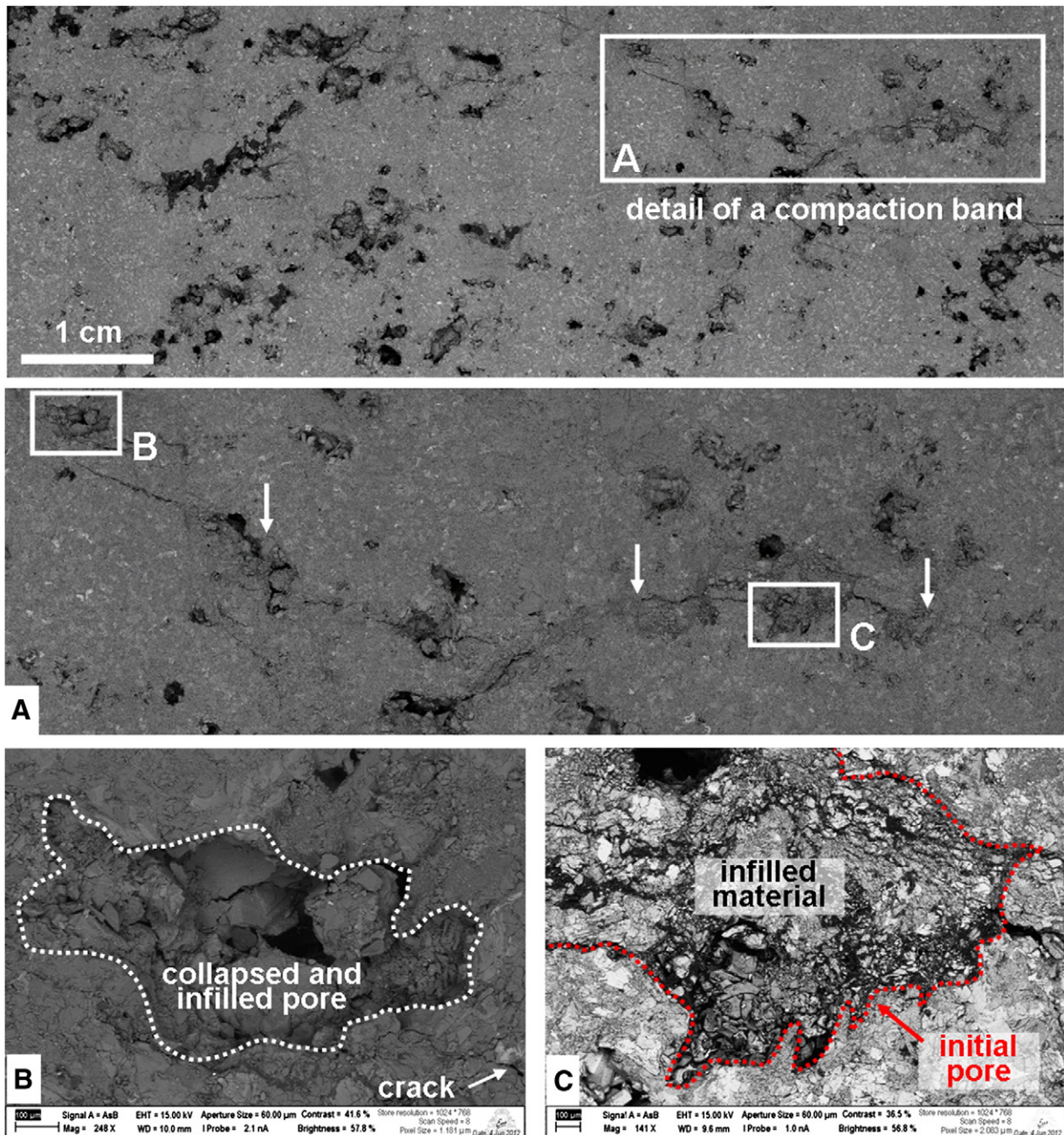

Fig. 13. SEM pictures taken on the sample deformed in test T2. The direction of main stress is vertical. A: Detail of a compaction band. B and C: Details of two collapsed pores infilled with crushed material. Note that picture B has been modified to enhance the contrast between former pore space and matrix.

4. Discussion

Our experimental data obtained on the Reykjanes basalt provide some indications about the yield envelope although this one has not been fully determined. Reykjanes basalt fails by brittle failure at low effective pressures. At higher effective pressures, localization of the deformation occurs in the form of subhorizontal bands. Figs. 10, 11 and 13 show that the deformation bands are not perfectly planar. This suggests that they may be partly composed of pure compaction segments and partly of shear segments. Moreover, the existence of both shear and compressive AE events within the localized deformation areas leads to conclude that, as in sandstones, probably a range of mixed mode of deformation regimes exist between pure shear failure and pure compaction bands (Issen and Rudnicki, 2000; Bésuelle, 2001). As basalt has a higher strength than sandstone and due to its lower porosity, the pure compressive domain is expected to occur at large confining pressure values, i.e. more than 100 MPa (not reached by our triaxial cell). In order to determine P^* (limit of the elastic domain for $Q = 0$), an isotropic loading of 200 MPa was performed but the regime remained elastic (Adelinet et al., 2010). The value P^* corresponds to the mean stress at the beginning of material crushing and pore collapse under hydrostatic pressure. If we make the assumption that the critical pressure P^* is primarily controlled by the porosity Φ and the grain size R (Wong et al., 1997; Wong and Baud, 1999), P^* can be expressed as $P^* \propto (\Phi R)^{-3/2}$. Based on pycnometry and SEM analysis, we assume that $\Phi \approx 0.1$ and that $R \approx 100$ μm (average size of microliths, see Fig. 2) for our basaltic sample. Indeed, we assume that microliths of the matrix play a key role in the failure processes. It results that $\Phi R \approx 10^{-2}$ mm. Note that the value of R is very close to the one of the Bentheim sandstone (Baud et al., 2004). If we follow the empirical law presented in Wong et al. (1997) for sandstones, we predict an approximate theoretical P^* value of about 400 MPa, which is relevant to what is observed on the Yakuno basalt which presents nearly the same microstructure (Shimada, 2000). This theoretical value is denoted in Fig. 14 as P_{th}^*, that is well beyond our experimental capabilities. The full shape of the yield envelope remains thus unknown (cf. Fig. 14). The parabolic envelope appears to be well constrained by the four points (T1, T2, T3 and T4). As we know that a mixed deformation regime appears close to $Q = 250$ MPa (T2), it is thus suggested that a cap exists between T3 and the theoretical critical pressure P_{th}^* (Wong et al., 1997; Issen and Rudnicki, 2000). Further experiments are required to check the existence of a cap envelope.

The deformation modes in basalt appear to be controlled by the original rock microstructure, and in particular by the equant porosity. The volatile exsolution from the basaltic melt phase leads to the formation of vesicles within the basalt. Some of them are connected by so thin cracks that mercury cannot reach them, that can explain the difference of about 2% between He-pycnometry and mercury porosimetry. This equant probably which is hardly accessible plays a key role in the formation of localized compaction areas. If we consider a mean value of grain size of 100 μm (feldspar microlites) and a mean value of equant pores of 500 μm, this ratio is about 1:5 whereas in sandstones it can reach 10:1. This ratio probably plays a role in the geometry of the localized compaction areas and in the threshold values of critical stress.

5. Related seismological implications

All our experiments have been performed at room temperature. To extrapolate the behavior of basalts to the Earth's interior, we keep in mind that temperature is a key parameter which plays a leading role. For instance, an increasing of temperature decreases the P^* point. Thus, (Violay et al., 2010, 2012) present very interesting experimental data on the brittle–ductile transition of basalt which are fully complementary to our results. However, the room-temperature behavior of basalt in terms of deformation have some interesting geological implications. Indeed, it is generally known that below a temperature of 200 °C the
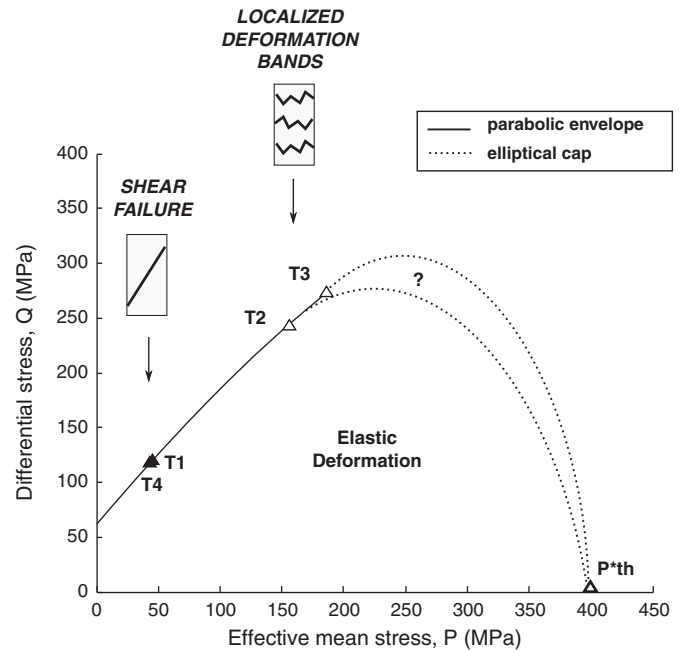

Fig. 14. Peak stress for brittle failure (solid symbols) and stress state C^* at the onset of shear compaction (open symbols) shown in the P (effective mean stress)–Q (differential stress) space.

micromechanisms of deformation remain the same without occurrence of crystal plasticity. Crustal oceanic earthquakes are widely explained to occur in the brittle part of the crust, and few historical earthquakes have been recorded after the brittle/ductile transition. Nevertheless, our experiments lead to high confining pressure – the equivalent of about 3 km depth – and show that pore collapse and associated crack formation in the ductile regime emit a lot of acoustic emissions. Furthermore, whereas an increase of the differential stress leads to a macroscopic failure in the brittle regime, no such consequence is observed in the ductile regime. Thus, if the porous state of basalt is preserved in depth, we can imagine that ductile deformation occurring at high depth within Icelandic basalt can induce some acoustic activities which could be considered as instabilities in the ductile crust. Yet, in the hydrothermal Icelandic context a lot of secondary phases may crystallize and fill the pore space.

6. Conclusion

The experimental results obtained in a triaxial cell on the Reykjanes basalt provide new insights on the deformation modes of basalt according to stress state. On the one hand, a classical brittle failure mode occurs at low effective pressure. On the other hand, subhorizontal deformation bands occur at higher effective pressure. Pure compaction bands have not been observed probably due to limited experimental conditions.

The deformation modes of porous rocks have important consequences for hydrodynamic properties. In a basaltic context, fluid flow is usually controlled by the macroscopic tectonic fractures which act as drain. Nevertheless at depths, where fractures are closed or inexistent, deformation of the basaltic matrix becomes important. Compaction bands can reduce or enhance the fluid flow at a reservoir scale. In any case, they control the ratio between horizontal and vertical permeability depending on their orientation. Our preliminary experimental study shows that such localized deformation bands could occur in basalt at confining pressure corresponding to an overburden of about 3 km depth. In hydrothermal volcanic areas, the development of localized deformation bands can strongly influence the fluid paths and consequently the localization of potential overpressure zones which can trigger fluid-driven earthquakes.

Acknowledgments

References

Adelinet, M., Fortin, J., Guéguen, Y., Schubnel, A., Geoffroy, L., 2010. Frequency and fluid effects on elastic properties of basalt: experimental investigations. Geophysical Research Letters 37. http://dx.doi.org/10.1029/2009GL041660.

Adelinet, M., Fortin, J., Guéguen, Y., 2011a. Dispersion of elastic moduli in a porous-cracked rock: theoretical predictions for squirt-flow. Techtonophysics 503, 173–181.

Adelinet, M., Dorbath, C., Le Ravalec, M., Fortin, J., Guéguen, Y., 2011b. Deriving microstructure and fluid state within the Icelandic crust from the inversion of tomography data. Geophysical Research Letters 38. http://dx.doi.org/10.1029/2010GL046304.

Baig, A., Urbancic, T., 2010. Microseismic moment tensors: a path to understanding frac growth. TLE 29, 320–324.

Balme, M.R., Rocchi, V., Jones, C., Sammonds, P.R., Meredith, P.G., Boon, S., 2004. Fracture toughness measurements on igneous rocks using a high-pressure, high-temperature rock fracture mechanics cell. Journal of Volcanology and Geothermal Research 132, 159–172.

Baud, P., Klein, E., Wong, T.-f., 2004. Compaction localization in porous sandstones: spatial evolution of damage and acoustic emission activity. Journal of Structural Geology 26.

Benson, P.M., Thompson, B.D., Meredith, P.G., Vinciguerra, S., Young, R., 2007. Imaging slow failure in triaxially deformed Etna basalt using 3D acoustic emission location and X-ray computed tomography. Geophysical Research Letters 34. http://dx.doi.org/10.1029/2006GLO28,721.

Benson, P.M., Vinciguera, S., Meredith, P.G., Young, R.P., 2008. Laboratory simulation of volcano seismicity. Science 322, 249.

Bésuelle, P., 2001. Compacting and dilating shear bands in porous rock. Journal of Geophysical Research 106, 13,435–13,442.

Brantut, N., Schubnel, A., Guéguen, Y., 2011. Damage and rupture dynamics at the brittle–ductile transition. Journal of Geophysical Research 116. http://dx.doi.org/10.1029/2010JB007675.

Cordonnier, B., Hess, K.U., Lavallee, Y., Dingwell, D.B., 2009. Rheological properties of domes lavas: case study of Unzen volcano. EPSL 279, 263–272.

D'Ozouville, N., Auken, E., Sorensen, K., Violette, S., de Marsily, G., Deffontaines, B., Merlen, G., 2008. Extensive perched aquifer and structural implications revealed by 3D resistivity mapping in a Galapagos volcano. EPSL 269, 518–522.

Fortin, J., Schubnel, A., Guéguen, Y., 2005. Elastic wave velocities and permeability evolution during compaction of Bleurswiller sandstone. Rock Mechanics and Rock Engineering 42, 873–889.

Fortin, J., Stanchits, G., Dresen, S., Guéguen, Y., 2006. Acoustic emission and velocities associated with the formation of compaction bands in sandstone. Journal of Geophysical Research 111 (B10), 203. http://dx.doi.org/10.1029/2005JB003854.

Fortin, J., Stanchits, S., Dresen, G., Guéguen, Y., 2009. Acoustic emissions monitoring during inelastic deformation of porous sandstone: comparison of three modes of deformation. Pure and Applied Geophysics 166, 823–841.

Fortin, J., Stanchits, S., Vinciguerra, S., Guéguen, Y., 2011. Influence of thermal and mechanical cracks on permeability and elastic wave velocities in a basalt from Mt. Etna volcano subjected to elevated pressure. International Journal of Rock Mechanics and Mining 503, 60–74.

Geoffroy, L., Dorbath, C., 2008. Deep downward fluid percolation driven by localized crust dilatation in Iceland. Geophysical Research Letters 35.

Goldberg, D., Takahashi, T., Slagle, A., 2008. Carbon dioxide sequestration in deep-sea basalt. Proceedings of the National academy of Sciences of the United States of America 105, 9920–9925.

Handin, J., Hager, R.V., 1963. Experimental deformation of sedimentary rocks under confining pressure: pore pressure tests. AAPG Bulletin 47.

Heap, M., Vinciguerra, S., Meredith, P., 2009. The evolution of elastic moduli with increasing crack damage during cyclic stressing of a basalt from Mt Etna volcano. Tectonophysics 471, 153–160.

Heap, M., Baud, P., Meredith, P., Vinciguerra, S., Bell, A.F., Main, I., 2011. Brittle creep in basalt and its application to time-dependent volcano deformation. EPSL. http://dx.doi.org/10.1016/j.epsl.2011.04.035.

Hudson, J., Pearce, R., Rogers, R., 1989. Source type plot for inversion of the moment tensor. Journal of Geophysical Research 94, 765–774.

Issen, K.A., Rudnicki, J.W., 2000. Conditions for compaction bands in porous rock. Journal of Geophysical Research 105, 21529–21535.

Kato, A., Sakaguchi, A., Yoshida, S., Mochizuki, H., Kaneda, Y., 2003. Permeability measurements and precipitation sealing of basalt in an ancient exhumed subduction-zone fault. Bulletin Earthquake Research Institute 78, 83–89.

Klein, E., Baud, P., Reuschlé, T., Wong, T.f., 2001. Mechanical behaviour and failure mode of Bentheim sandstone under triaxial compression. Physics and Chemistry of the Earth, Part A 26, 21–25.

Lore, J., Gao, H., Aydin, A., 2000. Viscoelastic thermal stress in cooling basalt flows. Journal of Geophysical Research 105, 23,695–23,709.

Matter, J., Takahashi, T., Goldberg, D., 2007. Experimental evaluation of in situ CO_2–water–rock reactions during CO_2 injection in basaltic rocks implications for geological CO_2 sequestration. G3 8.

Ougier-Simonin, A., Fortin, J., Guéguen, Y., Schubnel, A., Bouyer, F., 2011. Cracks in glass under triaxial conditions. International Journal of Engineering Science 49 (1), 105–121.

Papka, S.D., Kyriakides, S., 1998. Biaxial crushing of honeycombs — part I: experiments. International Journal of Solids and Structures 36, 4367–4396.

Paterson, M.S., 1978. Experimental Rock Deformation: The Brittle Field. Springer, New York.

Pinkerton, H., Norton, G., 1995. Rheological properties of basaltic lavas at sub-liquidus temperatures: laboratory and field measurements on lavas from Mount Etna. Journal of Volcanology and Geothermal Research 68, 307–323.

Ramsey, J.M., Chester, F.M., 2004. Hybrid fracture and the transition from extension fracture to shear fracture. Nature 428, 63–66.

Rocchi, V., Sammonds, P.R., Kilburn, C.R.J., 2002. Flow and fracture maps for basaltic rock deformation. Journal of Volcanology and Geothermal Research 120, 25–42.

Rocchi, V., Sammonds, P.R., Kilburn, C.R.J., 2004. Fracturing of Etnean and Vesuvian rocks at high temperature and low pressure. Journal of Volcanology and Geothermal Research 132, 137–157.

Saar, M.O., Manga, M., 1999. Permeability–porosity relationship in vesicular basalts. Geophysical Research Letters 26, 111–114.

Schubnel, A., Thompson, B.D., Fortin, J., Guéguen, Y., Young, R.P., 2007. Fluid-induced rupture experiment on fontainebleau sandstone: premonitory activity, rupture propagation, and aftershocks. Geophysical Research Letters 34. http://dx.doi.org/10.1029/2007GL031076.

Secor, D., 1965. Role of fluid pressure in jointing. American Journal of Science 263, 633–646.

Shimada, M., 2000. Mechanical behavior of rocks under high pressure conditions. Geomechanics Research Series 2.

Sigurdsson, O., Gudmundsson, A., Fridleifsson, G.O., Franzon, H., Gudlaugsson, S.P., Stefansson, V., 2000. Database on igneous rock properties in Icelandic geothermal systems. Status and unexpected results. Proc. World. Geotherm. Congr.

Smith, R., Sammonds, P., Kilburn, R., 2009. Fracturing of volcanic systems: experimental insights into pre-eruptive conditions. EPSL 280, 211–219.

Stanchits, S., Vinciguerra, S., Dresen, G., 2006. Ultrasonic velocities, acoustic emission characteristics and crack damage of basalte and granite. Pure and Applied Geophysics 163, 1–20.

Vajdova, V., Baud, P., Wong, T.-f., 2004. Compaction, dilatancy, and failure in porous carbonate rocks. Journal of Geophysical Research 109. http://dx.doi.org/10.1029/2003JB002508.

Vinciguerra, S., Trovato, C., Meredith, P.G., Benson, P.M., 2005. Relating seismic velocities, thermal cracking and permeability in Mt. Etna and Iceland basalts. Rock Mechanics and Rock Engineering 42, 900–910.

Violay, M., Gibert, B., Mainprice, D., Evans, B., Pezard, P., Flovenz, O.G., Asmundsson, R., 2010. The brittle ductile transition in experimentally deformed basalt under oceanic crust conditions: evidence for presence of permeable reservoirs at supercritical temperatures and pressures in the Icelandic crust. Proc. World. Geotherm. Congr.

Violay, M., Gibert, B., Mainprice, D., Evans, B., Dautria, J.M., Azais, P., Pezard, P., 2012. An experimental study of the brittle–ductile transition of basalt at oceanic crust pressure and temperature conditions. Journal of Geophysical Research 117, B03213. http://dx.doi.org/10.1029/2011JB008884.

Wong, T.-f, Baud, P., 1999. Mechanical compaction of porous sandstone. Oil Gas Science and Technology 54, 715–727.

Wong, T.-f, David, C., Zhu, W., 1997. The transition from brittle faulting to cataclastic flow in porous sandstone: mechanical deformation. Journal of Geophysical Research 102, 3,009–3,025.

Wong, T.f., Baud, P., Klein, E., 2001. Localized failure modes in a compactant porous rock. Geophysical Research Letters 28, 2521–2524.